(Received 9 June 2025, Accepted 25 July 2025, Scheduled 3 August 2025)

A Racket-Shaped UWB MIMO Antenna Based on Characteristic Mode Analysis

Zhonggen Wang[1], Fukuan Zhang[1], Wenyan Nie[2,*], Ming Yang[3], and Chenlu Li[4]

[1] School of Electrical and Information Engineering, Anhui University of Science and Technology, Huainan 232001, China
[2] School of Mechanical and Electrical Engineering, Huainan Normal University, Huainan 232001, China
[3] School of Electrical and Communications Engineering, West Anhui University, Lu'an 237012, China
[4] School Electrical and Information Engineering, Hefei Normal University, Hefei 230061, China

ABSTRACT: In this paper, a racket-shaped ultra-wideband (UWB) multiple-input multiple-output (MIMO) antenna is analytically designed using characteristic mode analysis. The antenna has an overall size of $60 \times 60 \times 1.6\,\text{mm}^3$ and consists of four racket-type radiating elements, four ground planes shaped like the number 6, and a cross-shaped decoupling structure between the radiating units. In the single antenna configuration, the feed position is determined by analyzing the current and electric field distributions of its characteristic modes. The bandwidth and current distribution are optimized by integrating seven small rings, L-shaped branches, and etched slots to ensure the simultaneous excitation of six characteristic modes, thereby enabling its UWB performance. In the MIMO setup, four elements are orthogonally arranged, and a cross-shaped decoupling structure along with a defected ground structure is employed to reduce mutual coupling, achieving over 20 dB isolation between any two elements. Simulated and measured results confirm that the antenna operates over the 3–21 GHz range, fully encompassing the UWB range of 3.1–10.6 GHz. Furthermore, the antenna achieves up to 77% radiation efficiency, a peak gain of 5.75 dBi, and a low envelope correlation coefficient (ECC).

1. INTRODUCTION

In recent years, UWB MIMO antennas have been widely applied in wireless systems, including radar detection, microwave imaging, and medical monitoring [1–3]. The integration of UWB and MIMO technologies offers enhanced bandwidth, increased data rates, and reduced latency. Moreover, it also mitigates multipath fading and enhances channel capacity [4].

For UWB MIMO antennas, the key characteristics such as compactness, bandwidth, and isolation are of primary concern. Extensive research has yielded various strategies for enhancing these aspects [5–12]. Common isolation techniques include defected ground structure (DGS) [13], decoupling networks [14], and neutralization lines [15], while approaches to realize UWB characteristics involve gradient geometries [16], resonant structures [17], and slot-based designs [18]. Ref. [11] introduces a frog-shaped UWB MIMO antenna comprising two frog-shaped monopoles and a partially etched ground plane. A T-shaped ground with dual T-slots suppresses coupling currents, resulting in isolation levels below -17 dB across the entire band and under -20 dB within the 5G range. In [13], a multi-band antenna is formed by embedding four square-slotted circular patches with integrated microstrip feeders and rectangular slots. The addition of DGS further enhances isolation. Ref. [14] presents a MIMO antenna employing a π-shaped transmission-line-based decoupling network, achieving up to 37 dB isolation at 3.6 GHz within the 3.4–3.8 GHz band. The antenna in [15] consists of two side-by-side elements decoupled by a meandering neutralization line, yielding 16 dB isolation. In [16], a compact stepped transmission-line-loaded antenna enables the multi-resonant operation of a square-slot structure across 2.1–11.5 GHz. Ref. [17] presents a metal slot array antenna employing a hybrid resonant configuration that excites five resonant modes via careful cavity and slot design, covering 7.35–10.05 GHz. Finally, [18] describes a novel millimeter-wave UWB antenna spanning 24.5–50 GHz, where a microstrip feed couples energy through a slot to a patch, quasi-monopole, and short strips, achieving wide-band, low-profile, and stable radiation performance.

Although various techniques discussed above can be applied to UWB MIMO antenna design, many existing designs still rely on trial-and-error processes, often lacking theoretical guidance and physical insight. In contrast, characteristic mode analysis (CMA) enables purposeful structural optimization and provides a clear understanding of modal behavior, thereby improving antenna performance [19–28]. Ref. [19] introduces a low-profile, broadband circularly polarized antenna comprising multiple patch cells and an L-shaped strip with three branches. The combined configuration excites four linearly polarized modes, which are shifted to desired frequencies via CMA, enabling broadband operation. In [20], a grounded antenna with a probe-fed sandwich structure is proposed; CMA reveals the excitation of quasi TM_{01} and TM_{02} modes, yielding monopole-like patterns and low cross-polarization over a wide band. Ref. [21] employs mode analysis to design a stacked U-groove patch antenna. Optimizing the coupling between the U-groove and

* Corresponding author: Wenyan Nie (wynie5240@163.com).

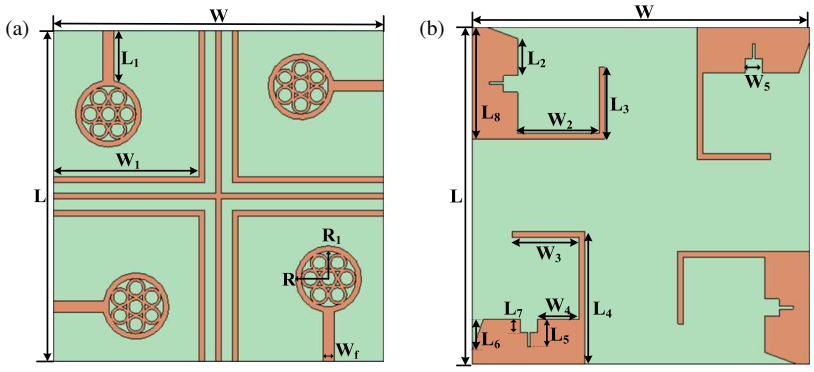

FIGURE 1. The proposed UWB MIMO antenna structure. (a) Top view, (b) bottom view.

stacked patches enables the excitation of five modes, resulting in a measured bandwidth of 52.7%. Ref. [22] develops a monopole-like patch antenna by combining two novel cavity modes. CMA shows that the resonant frequencies are tunable via four radial shorting pin arrays and slots. Modal currents and fields are analyzed, and coplanar waveguide T-junctions are used to excite desirable modes and suppress unwanted ones, resulting in broadband characteristics. Ref. [23] employs characteristic mode analysis to propose a three-band circularly polarized bidirectional microstrip metasurface antenna. CMA on 3×2 metasurface units guides the replacement of rectangular elements with curved rings and the modification of edge structures to suppress reverse currents and achieve circular polarization. Additionally, CMA is applied to metasurface units with integrated feed slots to excite resonance modes and realize three-band operation. Ref. [24], based on characteristic mode theory, utilizes an aperture-coupled feeding structure comprising L-shaped slots and microstrip lines to excite two orthogonal modes, thereby achieving circularly polarized radiation. In [25], a T-coupled feed is derived by analyzing characteristic modes. A ring ground structure introduces new resonances, and etched rectangular slots alter current paths, shifting high-frequency modes upward and enabling coverage of Bluetooth/Wi-Fi and N78 bands. Ref. [26] explores metasurface radiation characteristics via feature mode analysis to guide the design of a broadband omnidirectional metasurface antenna. The resulting antenna achieves a 70.1% bandwidth and exhibits a stable omnidirectional radiation pattern. Ref. [27] proposes a compact dual-polarized antenna with wide bandwidth and high isolation, where CMA is employed to suppress higher-order modes by narrowing the patch center and incorporating a U-shaped slot into the L-shaped probe. In [28], CMA is used to optimize antenna performance through modal significance, characteristic angle, and eigenvalue analysis. Currents on the metasurface and patch are also evaluated to target specific frequency bands.

In summary, this paper presents a novel UWB MIMO antenna comprising four racket-shaped radiating elements and four DGS with integrated L-shaped branches. Bandwidth and isolation are enhanced through the incorporation of a crosshair decoupling structure, additional L-shaped branches between elements, and etched stepped rectangular and triangular slots on the DGS. The antenna operates from 3 to 21 GHz, fully encompassing the UWB range with isolation exceeding 20 dB throughout, a peak gain of 6 dBi, and favorable radiation and diversity performance. Furthermore, the antenna's evolution is guided by CMA. By analyzing the modal current and electric field distributions, the feed point is confirmed at the rectangular microstrip line of radiating element, ensuring the simultaneous excitation of six characteristic modes and enabling effective UWB operation.

2. ANTENNA DESIGN AND ANALYSIS

2.1. Antenna Structure

The proposed antenna structure is illustrated in Figure 1. It is fabricated on an FR4 substrate with overall dimensions of $60 \times 60 \times 1.6\,\text{mm}^3$, a relative permittivity of 4.4, and a loss tangent of 0.02. Each of the four racket-shaped radiating elements comprises one large ring and seven small rings, with the small rings having an inner diameter of 1.5 mm, an outer diameter of 1.7 mm, and a center-to-center spacing of 3.3 mm. Both the crosshair segments and L-shaped branches have a width of 1 mm and are spaced 2 mm apart. These structures enhance both inter-element isolation and impedance matching. Additionally, a stepped rectangular slot and a triangular slot are etched on the DGS to further expand bandwidth and reduce coupling. Specifically, the width of the second slot within the stepped rectangular structure is 0.5 mm. Table 1 lists the detailed geometrical parameters of the antenna.

2.2. Design and Analysis of a Single Antenna Based on Characteristic Mode

Figure 2 illustrates the structural evolution of a single antenna, while the corresponding simulated S-parameters are presented in Figure 3. The antenna is fabricated on an FR4 substrate with dimensions of $30 \times 30 \times 1.6\,\text{mm}^3$. The evolved structure was modeled, and CMA was conducted using Computer Simulation Technology (CST) commercial software. The modal significance (MS) and characteristic angle (CA) of Antenna 1 are shown in Figure 4, and the modal current distributions at resonance are depicted in Figure 5. MS represents the contribution of each mode within a specific frequency range. An MS

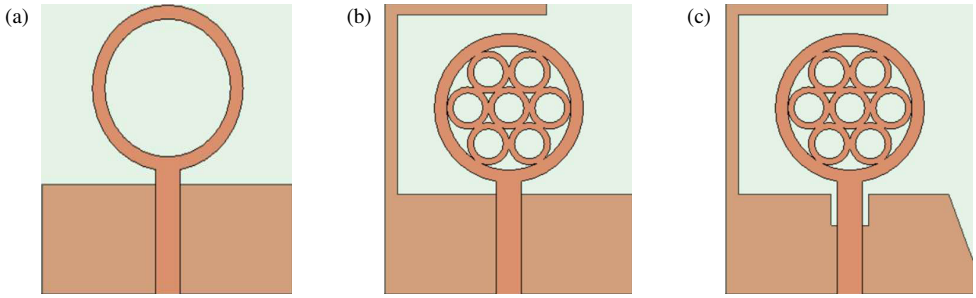

FIGURE 2. Structural evolution of a single antenna. (a) Antenna 1, (b) Antenna 2, (c) Antenna 3.

TABLE 1. Parametric dimensions of the antenna.

Parameters	W	L	W_1	L_1	W_2	L_2	W_3	L_3	R
Value (mm)	60	60	26.5	9.1	14.5	6.5	12	13	6
Parameters	W_4	L_4	W_5	L_5	W_f	L_6	L_7	L_8	R_1
Value (mm)	7.5	23.5	3	5	2	5.5	2.5	20	5

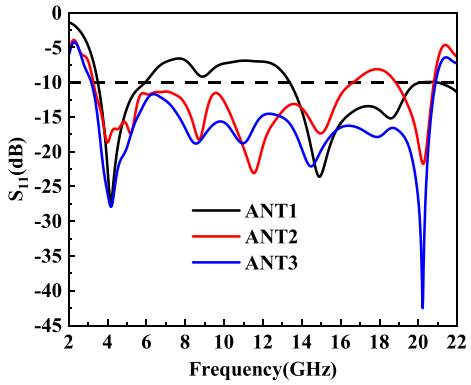

FIGURE 3. Simulated S-parameter plot of the antenna.

value approaching 1 indicates that the mode is more likely to be excited under suitable excitation, whereas an MS below 0.707 suggests limited resonance likelihood. CA indicates the resonance behavior of the mode; values near 180° correspond to stronger resonance conditions.

As shown in Figure 4, among the 12 characteristic modes, modes 1, 2, 5, 6, 9, and 10 can be theoretically excited under appropriate excitation. However, Figure 5 reveals that the currents of modes 5, 6, and 9 are mainly distributed on the circular ring, rectangular microstrip line, and lower edge of the ground plane, respectively. These modes contribute minimally to the bandwidth due to their low current intensity and distance from the feed ports. In contrast, modes 1, 2, and 10 exhibit strong current concentrations on the feed line and adjacent ground regions, making them excitable; however, the bandwidth that they collectively support remains insufficient to meet UWB specifications. The S-parameter curves of Antenna 1 in Figure 3 indicate dual operating bands of 3.52–5.95 GHz and 13.38–20.23 GHz, confirming that the structure fails to meet UWB criteria. Therefore, the antenna is subsequently optimized, as illustrated in Figure 2(b).

Antenna 2 incorporates seven small rings and an L-shaped branch relative to Antenna 1, as shown in Figure 2(b). The L-shaped branch extends the current path and interacts with the currents in the small rings, enabling excitation of additional characteristic modes and improving the overall bandwidth toward UWB criteria. The MS and CA of Antenna 2 are presented in Figure 6, with corresponding mode current distributions shown in Figure 7. Compared to Antenna 1, Antenna 2 exhibits notable differences in modal shapes and effective bandwidth coverage. Specifically, the resonant frequency of mode 10 shifts downward to 6.24 GHz, but its current is primarily located on the circular ring and L-shaped branch, away from the feed point, and is therefore not excitable. Mode 1 shifts slightly upward overall with increased bandwidth; mode 2 retains its frequency but shows a modified high-frequency profile. Modes 5, 6, and 9 shift downward by 1.56 GHz, 1.74 GHz, and 2.62 GHz, respectively, and, as shown in Figure 7, can be excited due to their strong localization near the feed port. The combined effective bandwidth of these modes spans 3.2–17 GHz but still falls short of the full UWB range of 3.1–10.6 GHz. The S-parameters in Figure 3 indicate a 3.27–16.65 GHz band, an improvement over Antenna 1. However, the 3.1–10.6 GHz UWB specification is not fully satisfied; therefore, the structure of Antenna 2 is further refined.

To shift characteristic modes to lower frequencies and ensure their excitation, Antenna 3 incorporates a stepped rectangular slot and a triangular slot etched into the ground plane of Antenna 2, as shown in Figure 2(c). These modifications alter the current distribution, concentrating it near the feed ports and allowing simultaneous excitation of six modes. As a result, the effective bandwidth fully spans the 3.1–10.6 GHz UWB range, as demonstrated in Figures 8 and 9.

Figure 8 illustrates the modal significance and characteristic angle of the antenna, while Figure 9 shows the modal current

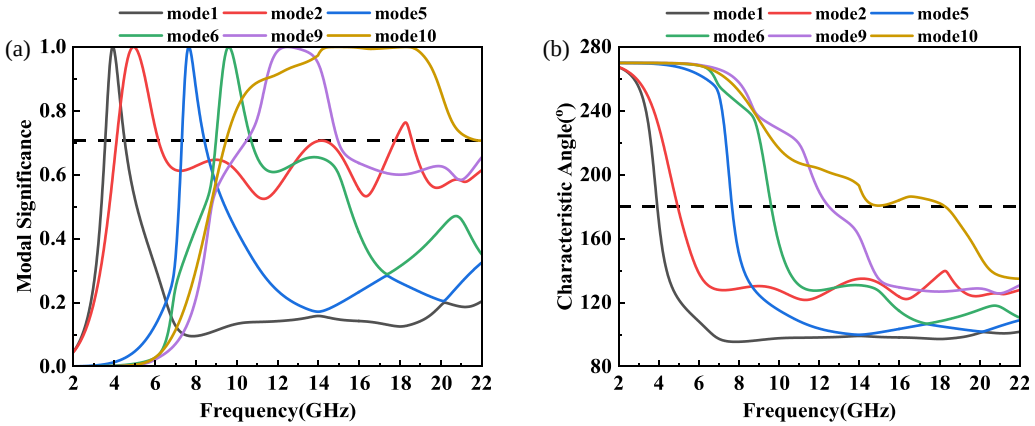

FIGURE 4. The simulated results of mode analysis of Antenna 1: (a) MS, (b) CA.

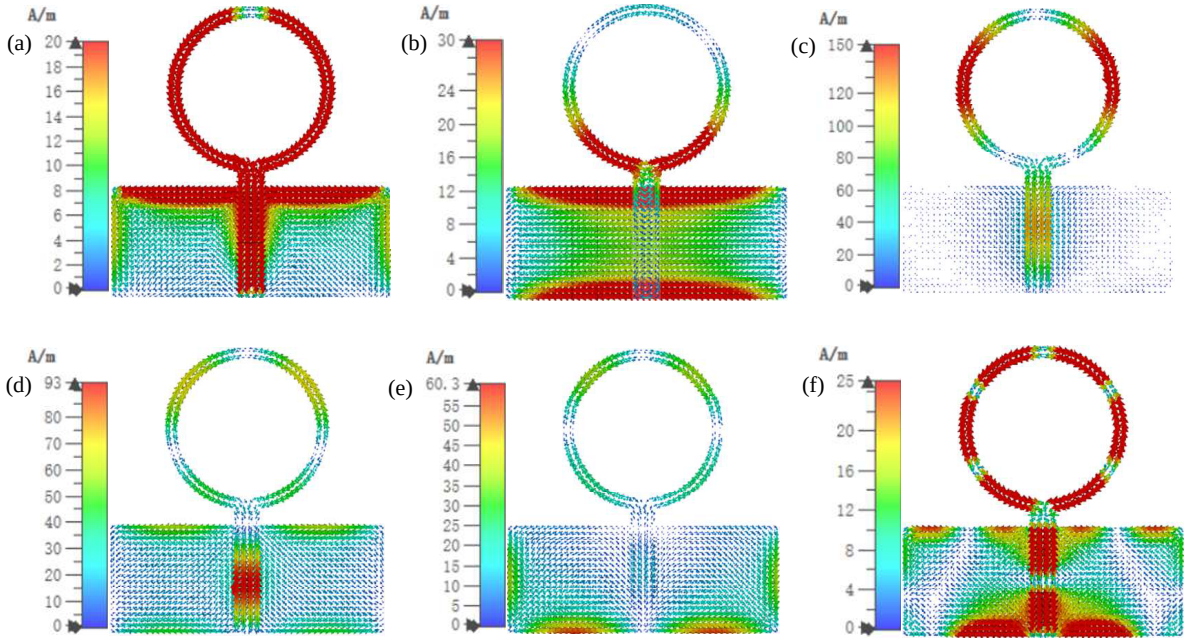

FIGURE 5. Simulated mode current distribution of Antenna 1: (a) mode 1 at 3.93 GHz, (b) mode 2 at 4.95 GHz, (c) mode 5 at 7.65 GHz, (d) mode 6 at 9.61 GHz, (e) mode 9 at 12.49 GHz, (f) mode 10 at 18.29 GHz.

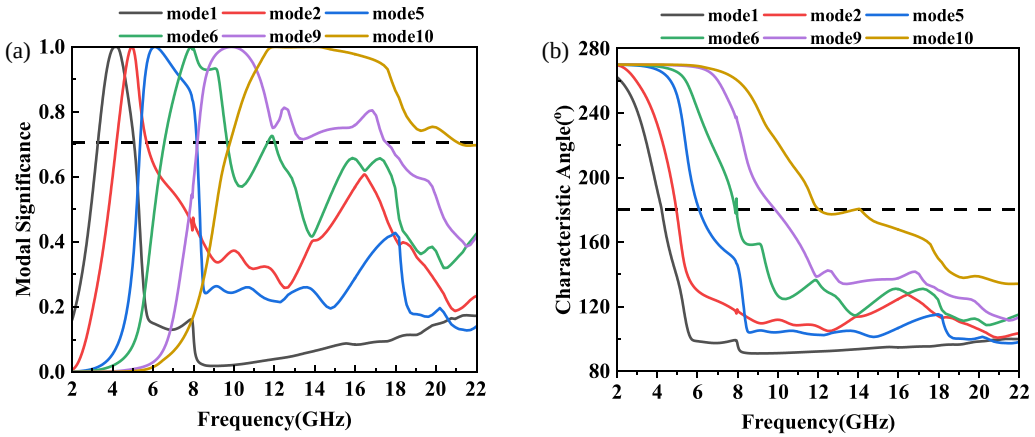

FIGURE 6. The simulated results of the mode analysis of Antenna 2: (a) MS, (b) CA.

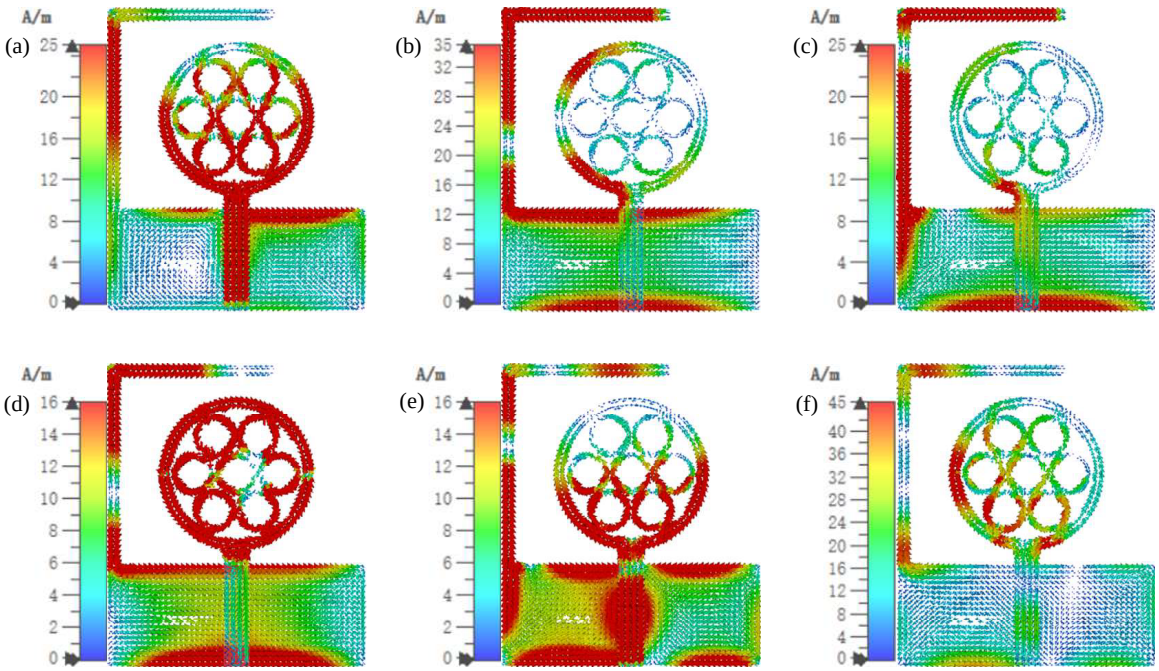

FIGURE 7. Mode current distribution of Antenna 2: (a) mode 1 at 4.23 GHz, (b) mode 2 at 4.95 GHz, (c) mode 5 at 6.09 GHz, (d) mode 6 at 7.87 GHz, (e) mode 9 at 9.87 GHz, (f) mode 10 at 12.05 GHz.

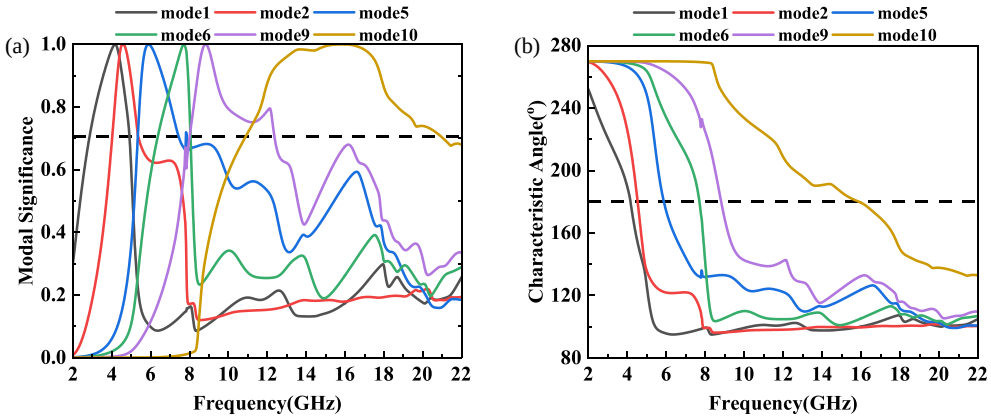

FIGURE 8. The simulated results of mode analysis of Antenna 3: (a) MS, (b) CA.

distributions at resonance. A comparison between Figures 9 and 7 reveals that etching the stepped rectangular and triangular slots enables excitation of mode 10, which was previously unexcited in Antenna 2, thereby broadening the bandwidth. Compared to Antenna 2, the resonant frequencies of modes 1, 2, 5, 6, and 9 in Antenna 3 shift downward, while mode 10 shifts upward by 3.89 GHz, with altered modal profiles. Figure 9 shows that the corresponding mode currents are enhanced and concentrated near the feed port, making them excitable. Figure 8 further indicates that the combined bandwidth of these modes fully spans the 3–21 GHz range, which is corroborated by the S-parameter results in Figure 3, where Antenna 3 also operates across this entire band.

2.3. MIMO Antenna Design and Analysis

The designed single antenna is symmetrically rotated about the center to form a four-element MIMO configuration, as shown in Figure 10(a). To further mitigate mutual coupling, an isolation branch is introduced, as illustrated in Figure 10(b). This branch comprises a central cross structure and four L-shaped elements. The impact of their spacing on isolation performance is discussed in Section 3.

Figure 11 presents a comparison of the S-parameters before and after incorporating the isolation branch. Figures 12 and 13 show the current distributions on Antenna models 4 and 5, respectively-without and with the isolation structure, both under port 1 excitation. Figure 11(a) shows that before adding the isolation structure, the resonant frequency is slightly shifted, mainly due to mutual interference and mismatch caused by radiator rotation and replication. After adding the isolation structure, the antenna's isolation performance is enhanced while its bandwidth remains unchanged. As illustrated in Figure 11(b), without the isolation branch, the overall isolation remains below 20 dB. This is further confirmed by Figure 12, which shows

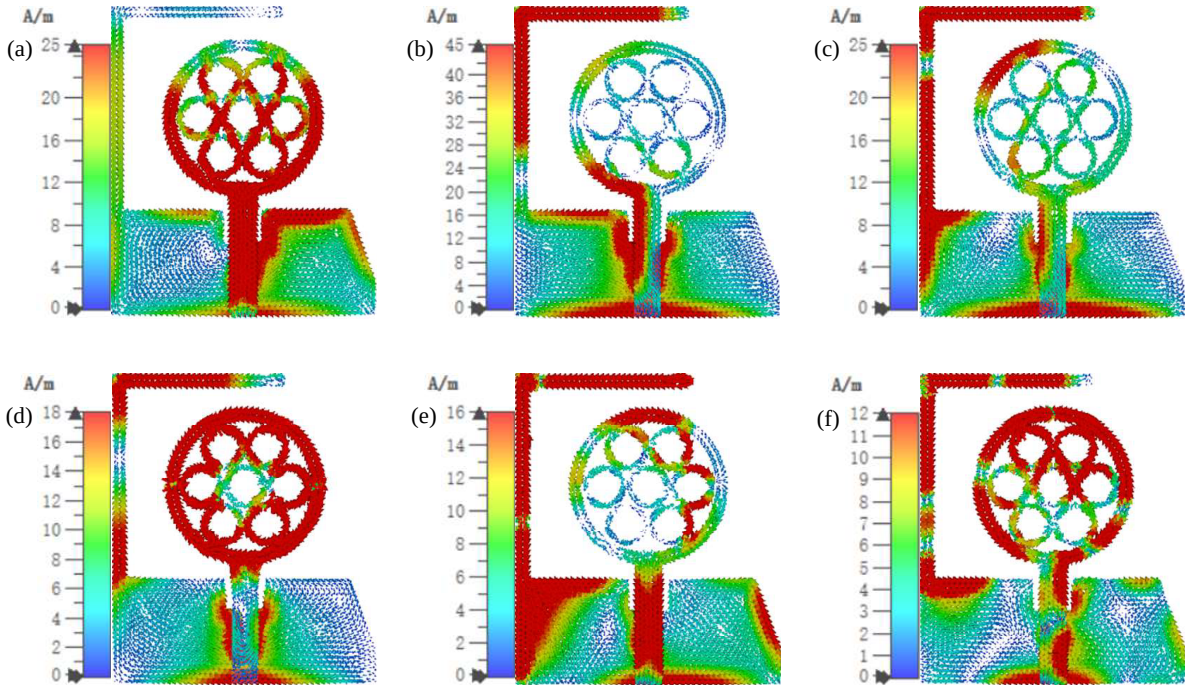

FIGURE 9. Simulated mode current distribution of Antenna 3: (a) mode 1 at 4.17 GHz, (b) mode 2 at 4.53 GHz, (c) mode 5 at 5.89 GHz, (d) mode 6 at 7.71 GHz, (e) mode 9 at 8.83 GHz, (f) mode 10 at 15.89 GHz.

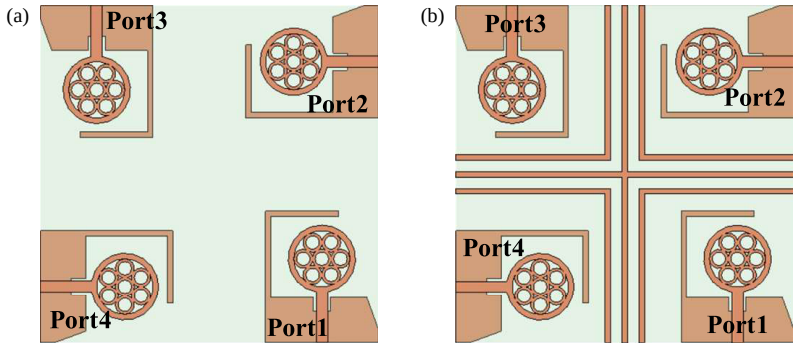

FIGURE 10. MIMO antenna design. (a) Antenna model 4. (b) Antenna model 5.

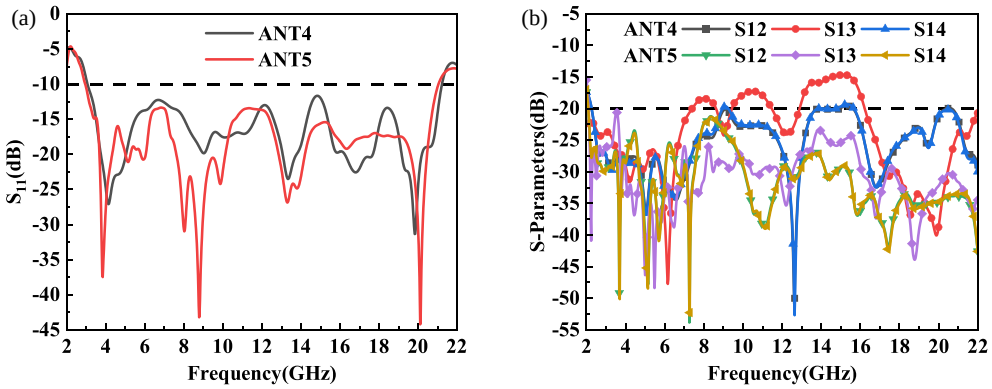

FIGURE 11. Simulated S-parameters before and after adding an isolated branch. (a) S_{11}, (b) S_{12}, S_{13} and S_{14}.

that although the defective ground structure blocks most current, residual coupling persists between the antenna elements, and both figures corroborate this observation. In contrast, Figure 13 demonstrates that the added isolation branch further suppresses residual coupling currents, significantly improving isolation. This improvement is corroborated by Figure 11(b), where the simulated S_{12}, S_{13}, and S_{14} rise to 21.2 dB, 20.5 dB, and 21.3 dB, respectively. The addition of isolation branches

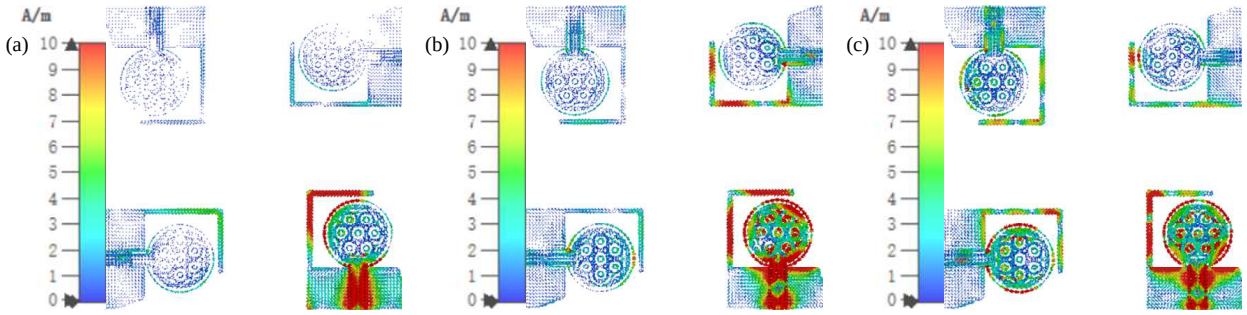

FIGURE 12. Simulated surface currents of antenna model 4. (a) 4.14 GHz, (b) 9.02 GHz, (c) 13.34 GHz.

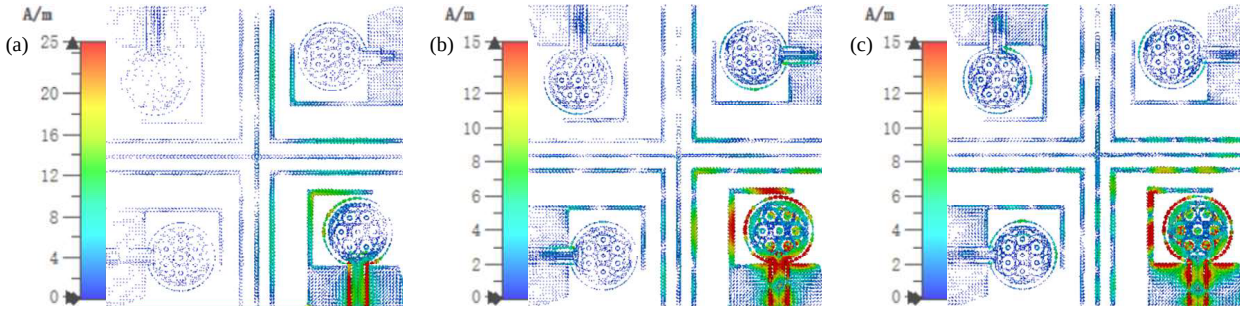

FIGURE 13. Simulated surface currents of antenna model 5. (a) 3.84 GHz, (b) 8.78 GHz, (c) 13.3 GHz.

not only enhances isolation and mitigates crosstalk, but also optimizes antenna performance, increases signal transmission capacity, and improves spectrum utilization.

2.4. Antenna Parameter Analysis

To investigate the impact of structural parameters on antenna performance, a systematic investigation was conducted. The objective was to evaluate how these parameters influence bandwidth and isolation. Specifically, the effects of the stepped slot width (W_5) and the gap between isolation structures were examined. W_5 was selected for its influence on bandwidth, while the spacing between isolation elements significantly affects both isolation and impedance matching.

The analysis process involves varying one parameter while keeping the others constant. The results are illustrated in the following figures. Figure 14 shows that increasing W_5 initially improves S_{11}; however, beyond 3 mm, S_{11} deteriorates, and the antenna becomes mismatched. Throughout the variation of W_5, S_{12}, S_{13}, and S_{14} remain largely unaffected, indicating that W_5 primarily affects bandwidth. Therefore, W_5 is set to 3 mm. Figure 15 indicates that the distance between isolation structures influences the resonance depth of S_{11} and has minimal impact on bandwidth, while significantly affecting the 4 GHz response of S_{13} in the high frequency region of S_{12}, S_{13}, and S_{14}. As the spacing increases, impedance matching improves, and the high-frequency response of the S-parameters is enhanced. Specifically, the 4 GHz notch of S_{13} approaches -20 dB. However, when the spacing exceeds 2 mm, impedance matching deteriorates. Thus, a spacing of 2 mm is selected based on overall performance.

3. RESULTS AND DISCUSSION

3.1. S-Parameters

To evaluate the antenna's practical performance, a prototype was fabricated as shown in Figure 16(a), and measurements were conducted in an anechoic chamber environment illustrated in Figure 16(b). The S-parameters were measured using an Agilent N52235A vector network analyzer, as shown in Figure 17. Figure 17 shows that the antenna operates across 3–21 GHz, fully encompassing the UWB of 3.1–10.6 GHz. Additionally, S_{12}, S_{13}, and S_{14} remain below -20 dB throughout the band, demonstrating effective isolation. The differences between simulated and measured results can be attributed to fabrication and soldering tolerances. Nevertheless, the results are generally consistent, confirming the antenna's stable performance.

3.2. Radiation Properties

Figure 18 shows the 3D radiation pattern of the antenna along with the 2D radiation patterns in the E-plane and H-plane at 3.84, 8.86, 13.23, and 20.12 GHz. As shown in the figure, the radiation patterns of the E-plane and H-plane at 3.84 GHz are nearly circular, demonstrating favorable omnidirectional performance. At 8.86 GHz, they exhibit a heart-like shape with near-omnidirectional behavior. At the resonance frequency of 13.33 GHz, the patterns show an irregular flower-like pattern, with main lobes directed at 30°–150° and 220°–330°, respectively. At 20.12 GHz, the radiation patterns exhibit an irregular flower-like structure, with primary lobes at 30°–120°, 180°–240°, and 270°–330°, confirming strong radiation capability.

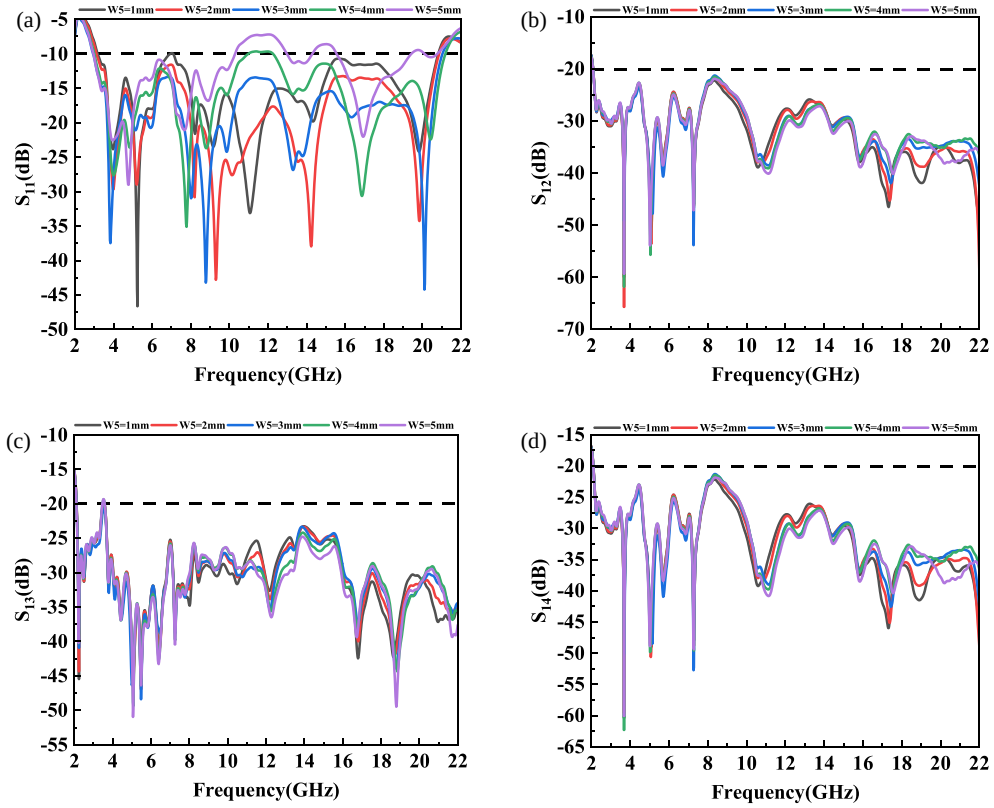

FIGURE 14. The effect of different W_5 lengths on antenna simulated S-parameters. (a) S_{11}, (b) S_{12}, (c) S_{13}, (d) S_{14}.

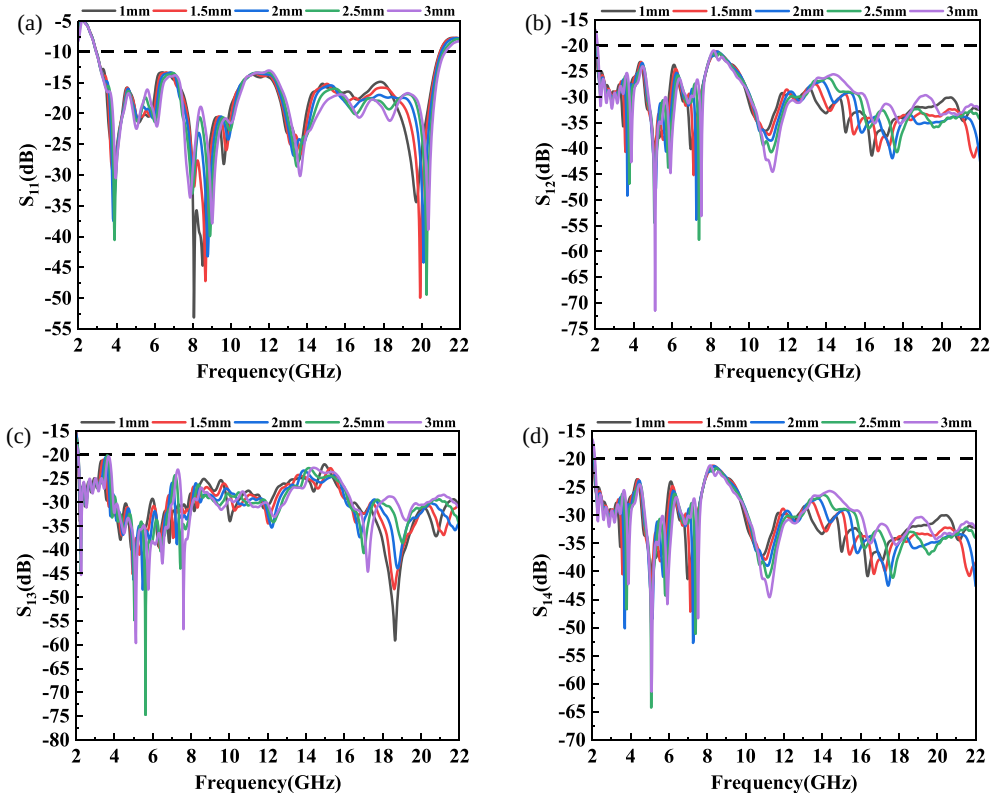

FIGURE 15. The effect of the distance between isolated branches on simulated S-parameters. (a) S_{11}, (b) S_{12}, (c) S_{13}, (d) S_{14}.

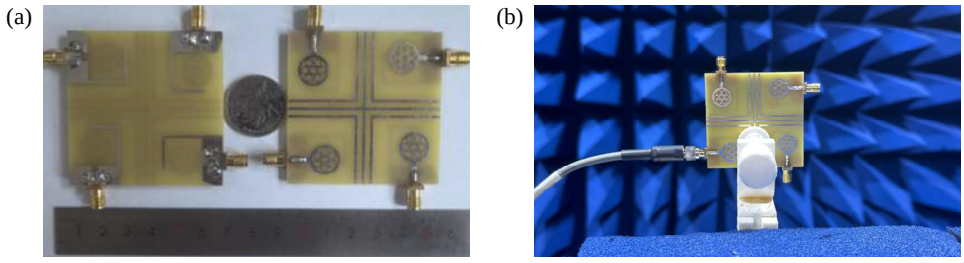

FIGURE 16. The proposed antenna. (a) Fabricated prototype and (b) S-parameters measurement environment.

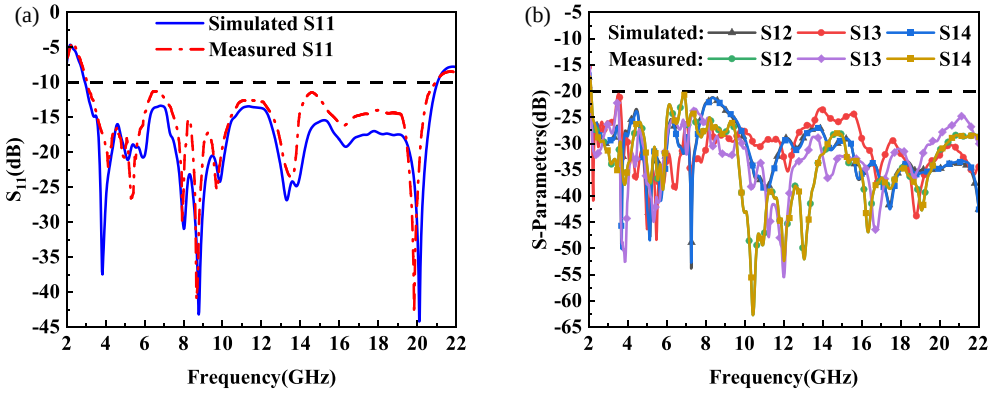

FIGURE 17. MIMO antenna simulated and measured S-parameters: (a) S_{11}, (b) S_{12}, S_{13}, and S_{14}.

Figure 19 shows the simulated and measured radiation efficiencies and peak gains of the antenna across the operating band. The antenna maintains a radiation efficiency of 50–77% across the full operating range and achieves a peak gain of 5.75 dBi. Overall, the actual measurement results of the two are consistent with the simulation ones.

3.3. MIMO Antennas Performance

Diversity performance metrics include envelope correlation coefficient (ECC), diversity gain (DG), total active reflection coefficient (TARC), channel capacity loss (CCL), and average effective gain ratio (MEG) [29]. These parameters assess the antenna's capability to deliver stable, high-quality, and uncorrelated signals and determine its suitability for UWB wireless communication links. This part was also simulated using CST electromagnetic software.

3.3.1. DG and ECC

ECC characterizes the correlation between signals received by different antenna elements in a MIMO system; lower ECC values indicate greater element independence. It is calculated using Equation (1), where ECC_{ij} represents the correlation between the ith and jth elements. DG measures signal enhancement in MIMO systems and is computed using Equation (2) [30]. For optimal diversity performance, ECC values should remain below 0.5, while DG values close to 10 indicate better diversity characteristics. Figure 20 shows the DG and ECC of the proposed MIMO antenna. Figure 20(b) shows that ECC remains below 0.0008 across the 3–21 GHz range, indicating strong isolation and minimal mutual coupling. As shown in Figure 20(a), the DG exceeds 9.997 across the full operating band, confirming the antenna's excellent diversity performance.

$$\mathrm{ECC}_{ij} = \frac{\left|\iint_{4\pi} \overrightarrow{F_i}(\theta,\phi) \cdot \overrightarrow{F_j^*}(\theta,\phi)\, d\Omega\right|^2}{\iint_{4\pi} \left|\overrightarrow{F_i}(\theta,\phi)\right|^2 d\Omega \cdot \iint_{4\pi} \left|\overrightarrow{F_j}(\theta,\phi)\right|^2 d\Omega} \tag{1}$$

$$\mathrm{DG}_{ij} = 10\sqrt{1-(\mathrm{ECC}_{ij})^2} \tag{2}$$

3.3.2. TARC and CCL

The efficiency of a MIMO antenna system can be evaluated using TARC. To ensure that the system exhibits low reflection loss, stable phase response, and reliable signal transmission, TARC is expected to remain below -10 dB. It is calculated as follows [29]:

$$\mathrm{TARC}_{ij} = -\sqrt{\frac{(S_{ii}+S_{ij})^2 + (S_{ji}+S_{jj})^2}{2}} \tag{3}$$

where TARC_{ij} denotes the TARC between the ith and jth antenna elements. Figure 21(a) shows that the TARC remains below -30 dB across 3–21 GHz, indicating minimal coupling, high channel independence, and enhanced system capacity within the MIMO system.

CCL is also an important parameter used to evaluate MIMO antenna systems; typically, when CCL is less than 0.5 bits/s/Hz,

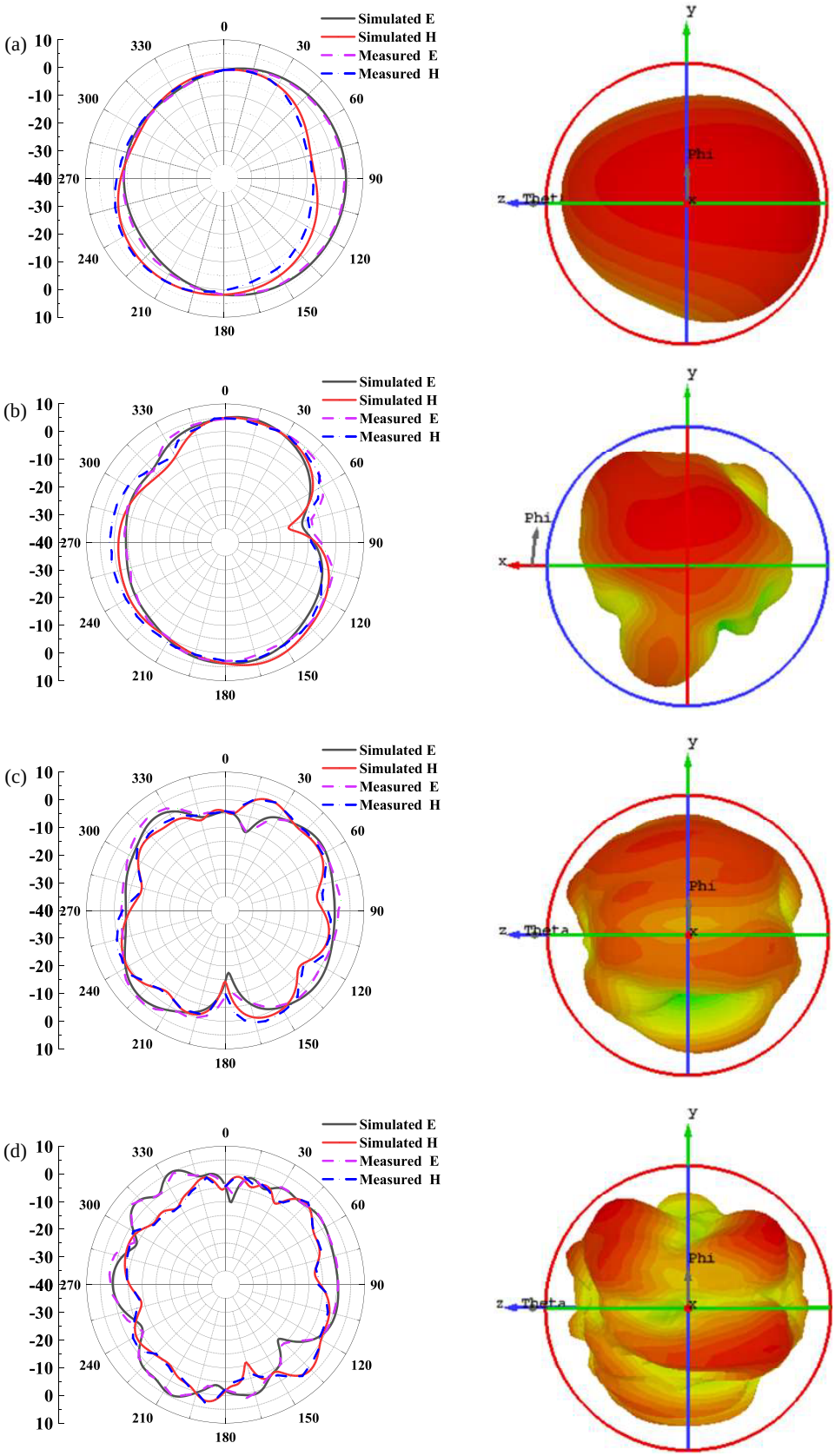

FIGURE 18. The simulated and measured two-dimensional radiation patterns and three-dimensional radiation patterns at (a) 3.84 GHz, (b) 8.86 GHz, (c) 13.23 GHz, and (d) 20.12 GHz.

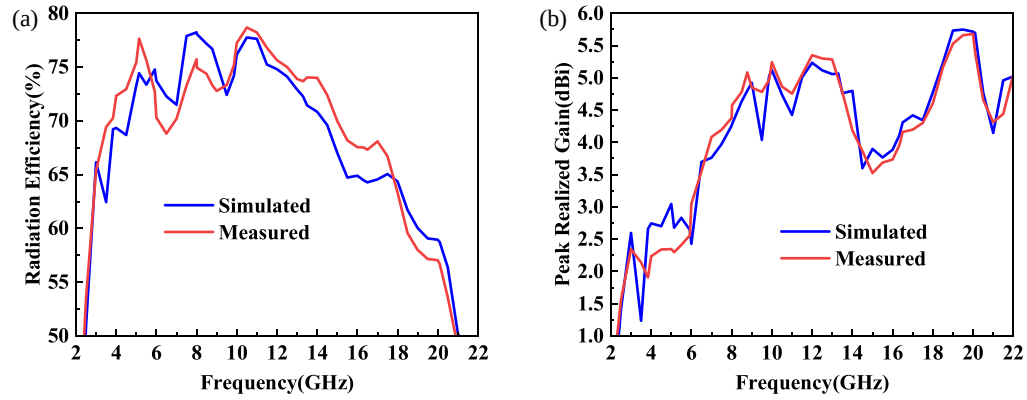

FIGURE 19. The measured and simulated radiation efficiencies and peak realized gains of the proposed antenna: (a) radiation efficiency and (b) peak realized gain.

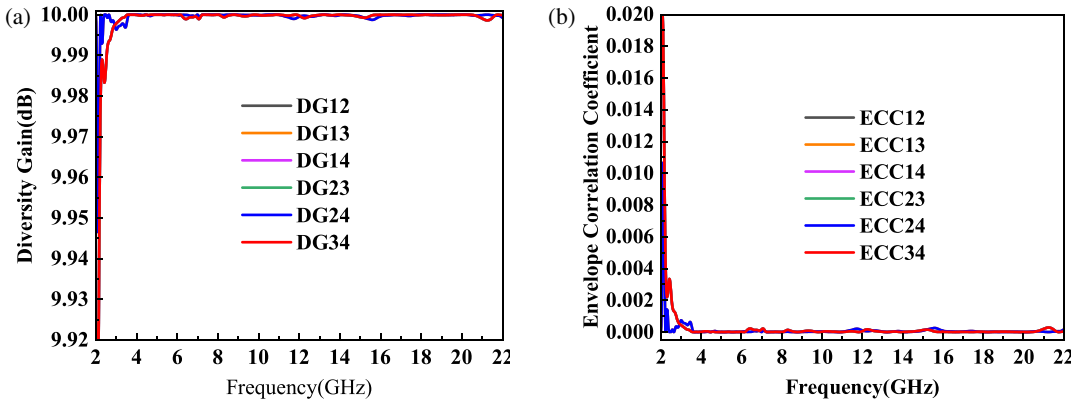

FIGURE 20. Simulated DG and ECC of the proposed antenna: (a) DG, (b) ECC.

the MIMO antenna system is regarded as meeting its performance requirements. These parameters are calculated using Equations (4)–(7) provided below [29]. α^R indicates the correlation matrix of the receiving antenna. As shown in Figure 21(b), the CCL is less than 0.4 bit/s/Hz, which indicates that the MIMO antenna system exhibits satisfactory performance.

$$\mathrm{CCL} = -\log_2 \det(\alpha^R) \tag{4}$$

$$\alpha^R = \begin{bmatrix} \alpha_{11} & \alpha_{12} & \alpha_{13} & \alpha_{14} \\ \alpha_{21} & \alpha_{22} & \alpha_{23} & \alpha_{24} \\ \alpha_{31} & \alpha_{32} & \alpha_{33} & \alpha_{34} \\ \alpha_{41} & \alpha_{42} & \alpha_{43} & \alpha_{44} \end{bmatrix} \tag{5}$$

$$\alpha_{mm} = 1 - \left| \sum_{n=1}^{4} S_{mn} \right| \tag{6}$$

$$\alpha_{mm} = -\left(S_{nm} * S_{mn} + S_{nm} * S_{mn}\right) \tag{7}$$

3.3.3. MEG

MEG is one of the key metrics used to evaluate MIMO antenna systems, and its calculation formula is shown in Equation (8) [31]. The data calculated from this formula are presented in Figure 22. This figure demonstrates that the antenna system exhibits favorable performance.

$$\mathrm{MEG}_{ij} = \frac{1 - \sum_{n=1}^{4} |S_{ni}|^2}{1 - \sum_{n=1}^{4} |S_{nj}|^2} \tag{8}$$

4. COMPARATIVE STUDY

Table 2 compares the proposed antenna with several existing designs in terms of size, bandwidth, isolation, ECC, radiation efficiency, isolation technology, and gain. As shown, the proposed antenna achieves the lowest ECC among all listed designs, indicating enhanced diversity capability. Compared to [1], it is larger but offers superior isolation and bandwidth. In comparison with [4], it exhibits lower isolation but features a smaller size and broader bandwidth. Compared to [6], it achieves higher gain and broader bandwidth while maintaining similar isolation. The antenna also outperforms [11] in terms of isolation and bandwidth. Although it has no size or gain advantage over [13], it shows a significant advantage in both isolation and bandwidth. Compared with [20] and [27], the proposed antenna provides a wider bandwidth. In terms of radiation efficiency, the proposed antenna exhibits superior per-

TABLE 2. Performance comparison of the proposed MIMO antenna with other antennas.

Ref.	CMA	Size (mm^2)	Bandwidth (GHz)	Isolation (dB)	Gain (dBi)	ECC	Radiation Efficiency (%)	Isolation Technology
[1]	No	36×36	2–11.08	> 15	3.5–6.5	< 0.13	> 70	Fan-shaped isolation
[4]	Yes	80×80	3.4–8.25	> 25	/	< 0.01	/	Plus shaped decoupling structure
[6]	No	29×50	2.4–11	> 20	0–2.5	< 0.04	> 40	/
[11]	No	31×55	3.05–13.38	> 17	2.25–5.75	< 0.007	> 89	DGS
[13]	No	39×39	3.96–6.12 9.42–20	> 11	6.6	< 0.018	/	Stepped decoupling slot and DGS
[20]	Yes	45×45	4.4–11.1	/	2.2–8.4	/	/	/
[27]	Yes	30×30	4.73–5.99	> 27.9	4.8–6.2	/	/	U-shaped trough
This work	Yes	60×60	3–21	> 20	1.25–5.75	< 0.0008	> 50	Cross-shaped decoupling structure

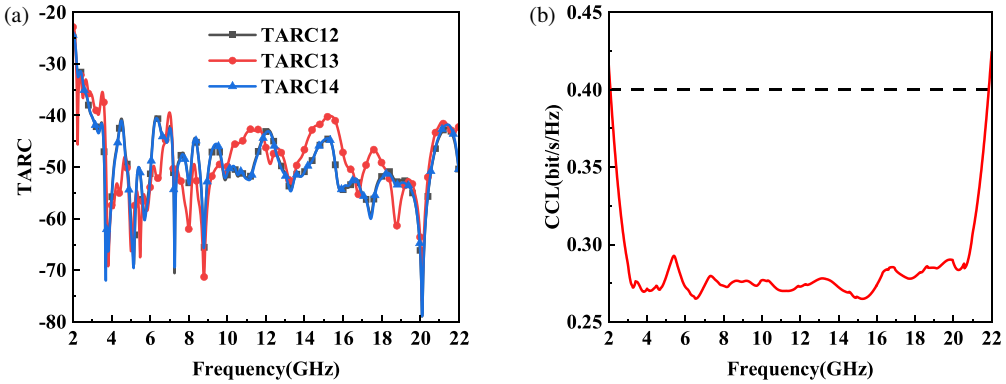

FIGURE 21. The simulated TARC and CCL of the proposed antenna: (a) TARC, (b) CCL.

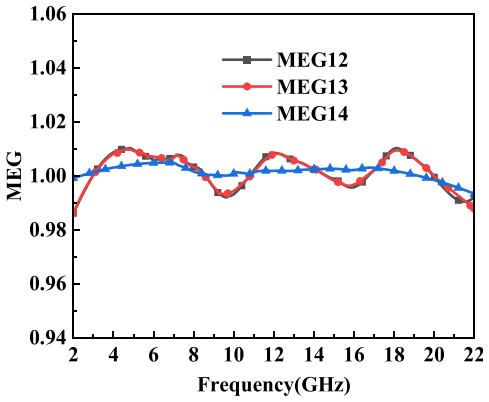

FIGURE 22. Simulated MEG ratio of the proposed antenna.

formance compared to [6]. In terms of isolation technology, the proposed antenna adopts a simpler design than the isolation structures used in [1, 11, 13], while achieving superior isolation performance. In summary, the proposed antenna demonstrates clear advantages in size, bandwidth, isolation, diversity characteristics, radiation efficiency, isolation technology, and radiation performance.

5. CONCLUSION

In this paper, a racket-shaped UWB MIMO antenna featuring a high isolation DGS is designed using CMA. During the single antenna evolution process, the structure is optimized by analyzing its characteristic modes and modal current distributions. Bandwidth and current coverage are enhanced by adding branches, ring elements, and etched slots to enable simultaneous excitation of six characteristic modes, thereby achieving UWB performance. Characteristic mode theory provides physical insight and guides structural optimization, resulting in an antenna comprising a racket-shaped radiator, DGS ground, and cross-shaped isolation structure. Stepped rectangular and triangular slots are etched on the ground alter current paths to enhance impedance matching and extend bandwidth. Additionally, the isolation structure comprising four L-shaped branches and a central cross further improves inter-element isolation, achieving values above 20 dB. Simulated and measured results confirm a bandwidth of 3–21 GHz, fully covering the UWB. The antenna also demonstrates a compact design, high radiation efficiency, and a low ECC. In the future, the antenna size could be further reduced without compromising overall perfor-

mance, enabling integration into miniaturized devices. Additionally, replacing the substrate with a flexible material would allow for wearable applications. In summary, the proposed antenna exhibits superior overall performance and is suitable for 5G, Wi-Fi 6E, and X-band applications.

ACKNOWLEDGEMENT

This work was supported by the Fund of Anhui Mining Machinery and Electrical Equipment Coordination Innovation Center (Anhui University of Science and Technology) under grant No. KSJD202406.

REFERENCES

[1] Ren, W., Z. Wang, M. Yang, J. Zhou, and W.-Y. Nie, "Design of a simple four-port UWB-MIMO antenna based on a fan-shaped isolator," *Progress In Electromagnetics Research M*, Vol. 126, 117–126, 2024.

[2] Fiser, O., V. Hruby, J. Vrba, T. Drizdal, J. Tesarik, J. Vrba Jr., and D. Vrba, "Uwb bowtie antenna for medical microwave imaging applications," *IEEE Transactions on Antennas and Propagation*, Vol. 70, No. 7, 5357–5372, 2022.

[3] Premkumar, M., A. Muthukrishnan, D. Srinivasan, *et al.*, "Design of circular ring shaped UWB antenna for BANs and MI applications," in *2023 9th International Conference on Advanced Computing and Communication Systems (ICACCS)*, 964–967, Coimbatore, India, 2023.

[4] Ghosh, A., A. Ghosh, and J. Kumar, "Circularly polarized wideband quad-element MIMO antenna with improved axial ratio bandwidth and mutual coupling," *IEEE Antennas and Wireless Propagation Letters*, Vol. 23, No. 12, 4718–4722, 2024.

[5] Yan, S., X. Zhai, H. Ren, and J. Zhang, "A low-profile dual-polarized omnidirectional antenna for WLAN/UWB applications," *IEEE Antennas and Wireless Propagation Letters*, Vol. 23, No. 5, 1433–1437, 2024.

[6] Potti, D., Y. Tusharika, M. G. N. Alsath, S. Kirubaveni, M. Kanagasabai, R. Sankararajan, S. Narendhiran, and P. B. Bhargav, "A novel optically transparent UWB antenna for automotive MIMO communications," *IEEE Transactions on Antennas and Propagation*, Vol. 69, No. 7, 3821–3828, 2021.

[7] Rajesh, G. and R. Poonkuzhali, "Design and analysis of CPW fed ultrathin flexible MIMO antenna for UWB and X-band applications," *IEEE Access*, Vol. 12, 96 704–96 717, 2024.

[8] Jayant, S. and G. Srivastava, "Close-packed quad-element triple-band-notched UWB MIMO antenna with upgrading capability," *IEEE Transactions on Antennas and Propagation*, Vol. 71, No. 1, 353–360, 2023.

[9] Yuan, W., J. Huang, X. Zhang, K. Cui, W. Wu, and N. Yuan, "Wideband pattern-reconfigurable antenna with switchable monopole and Vivaldi modes," *IEEE Antennas and Wireless Propagation Letters*, Vol. 22, No. 1, 199–203, 2023.

[10] Tangirala, G., S. Garikipati, D. M. K. Chaitanya, and V. K. Sharma, "High isolation four-port Wrench shaped compact UWB MIMO antenna for 3.1–10.6 GHz band," *Progress In Electromagnetics Research C*, Vol. 122, 67–82, 2022.

[11] Yao, S., T. Yang, X. Qiu, and X. Li, "A frog-shaped UWB MIMO antenna design for 5G," *Progress In Electromagnetics Research C*, Vol. 151, 101–112, 2025.

[12] Yao, Y., Y. Shao, J. Zhang, and J. Zhang, "A transparent antenna using metal mesh for UWB MIMO applications," *IEEE Transactions on Antennas and Propagation*, Vol. 71, No. 5, 3836–3844, 2023.

[13] Sreeramulu, K., S. T. Mahaboob, R. R. Reddy, and K. L. Kishore, "A square slotted circular patch MIMO antenna with DGS for UWB applications," in *2022 International Conference on Computing, Communication and Power Technology (IC3P)*, 94–97, Visakhapatnam, India, 2022.

[14] Yang, M., C. Liu, and X. Liu, "Design of π-shaped decoupling network for dual-polarized Y-probe antenna arrays," *IEEE Antennas and Wireless Propagation Letters*, Vol. 21, No. 6, 1129–1133, Jun. 2022.

[15] Du, C., Z. Zhao, X. Wang, and F.-H. Yang, "A compact CPW-fed triple-band MIMO antenna with neutralization line decoupling for WLAN/WiMAX/5G applications," *Progress In Electromagnetics Research M*, Vol. 103, 129–140, 2021.

[16] Paul, P. M., K. Kandasamy, M. S. Sharawi, and B. Majumder, "Dispersion-engineered transmission line loaded slot antenna for UWB applications," *IEEE Antennas and Wireless Propagation Letters*, Vol. 18, No. 2, 323–327, 2019.

[17] Sang, L., J. Wang, Z. Liu, W. Wang, W. Huang, and H. Tu, "A UWB metal waveguide slot array antenna based on hybrid resonant structural components," *IEEE Antennas and Wireless Propagation Letters*, Vol. 22, No. 4, 923–927, 2023.

[18] Li, J., Y. Zhu, Y. Shi, Y. Hu, and W. Hong, "Millimeter-wave ultrawideband antenna with hybrid-mode resonance including microstrip line, slot, patches, and quasi-monopole modes," *IEEE Antennas and Wireless Propagation Letters*, Vol. 23, No. 5, 1533–1537, 2024.

[19] Chen, W. H., L. H. Ye, K. Ding, F. Jiang, and D.-L. Wu, "A broadband circularly polarized antenna using characteristic mode analysis," *IEEE Transactions on Antennas and Propagation*, Vol. 72, No. 12, 9143–9151, 2024.

[20] Fu, C., C. Feng, W. Chu, Y. Yue, X. Zhu, and W. Gu, "Design of a broadband high-gain omnidirectional antenna with low cross polarization based on characteristic mode theory," *IEEE Antennas and Wireless Propagation Letters*, Vol. 21, No. 9, 1747–1751, 2022.

[21] Zeng, J., Z. Zhang, F. H. Lin, and F. Guan, "Penta-mode ultrawideband circularly polarized stacked patch antennas using characteristic mode analysis," *IEEE Transactions on Antennas and Propagation*, Vol. 70, No. 10, 9051–9060, 2022.

[22] Nie, L. Y., B. K. Lau, S. Xiang, H. Aliakbari, B. Wang, and X. Q. Lin, "Wideband design of a compact monopole-like circular patch antenna using modal analysis," *IEEE Antennas and Wireless Propagation Letters*, Vol. 20, No. 6, 918–922, 2021.

[23] Ren, M., J. Li, H. Zhao, and C. Xia, "A novel triband circularly polarized metasurface antenna based on characteristic mode analysis," *IEEE Antennas and Wireless Propagation Letters*, Vol. 23, No. 11, 3817–3821, 2024.

[24] Zhang, Z., Y. Cheng, H. Luo, and F. Chen, "Low-profile wideband circular polarization metasurface antenna with characteristic mode analysis and mode suppression," *IEEE Antennas and Wireless Propagation Letters*, Vol. 22, No. 4, 898–902, 2023.

[25] Wang, M., Z. Wang, M. Yang, W. Nie, and H. Lin, "Design of miniaturized tri-band wearable antenna based on characteristic mode theory," *Progress In Electromagnetics Research C*, Vol. 132, 187–203, 2023.

[26] Feng, G., Z. Wu, Y. Lu, J. Xu, S. Wang, and Z. Chen, "A wideband omnidirectional metasurface antenna using characteristic mode analysis," *IEEE Antennas and Wireless Propagation Letters*, Vol. 24, No. 2, 359–363, 2025.

[27] Zhan, Z., W. Huang, R. Deng, and B. Li, "Compact dual-polarized antenna with wide band and high isolation using characteristic mode analysis," *Progress In Electromagnetics Re-*

search C, Vol. 142, 95–106, 2024.

[28] Bhavani, K. D., B. T. P. Madhav, U. D. Yalavarthi, Y. Ramakrishna, and M. P. Raju, "Characteristic mode analysis for microstrip fed conformal metasurface multiband antenna," *Progress In Electromagnetics Research C*, Vol. 141, 1–11, 2024.

[29] Ren, W., Z. Wang, W. Nie, W. Mu, C. Li, and M. Wang, "A transparent ultra-wideband antenna fed by CPW based on characteristic mode theory," *Applied Computational Electromagnetics Society Journal (ACES)*, Vol. 39, No. 11, 987–998, 2024.

[30] Tao, Y., H. Lin, M. Yang, W. Nie, C. Li, and M. Wang, "Sickle-shaped tri-band MIMO antenna for 5G and X-band applications," *Progress In Electromagnetics Research C*, Vol. 147, 15–25, 2024.

[31] Islam, H., S. Das, T. Ali, T. Bose, S. Kumari, O. Prakash, and P. Kumar, "Bandstop filter decoupling technique for miniaturized reconfigurable MIMO antenna," *IEEE Access*, Vol. 10, 19 060–19 071, 2022.